ROTOR WAKE TAIL INTERACTIONS OF A HELICOPTER WIND TUNNEL MODEL WITH VARIOUS ROTOR HEAD CONFIGURATIONS

Ulrich Hartmann
M. Sc.
Chair of Aerodynamics and Fluid Mechanics
Technical University Munich, Germany

Christian Breitsamter
Prof. Dr.-Ing.
Chair of Aerodynamics and Fluid Mechanics
Technical University Munich, Germany

ABSTRACT

Experimental investigations are conducted on a twin-engine light utility helicopter wind tunnel model across various angles of attack. Six transient pressure transducers are installed on the vertical fin to examine the impingement effect of the wake of three rotor head configurations on the vertical tail. The analysis encompassed the root-mean-square (rms) values of surface pressure fluctuations and power spectral densities (PSD) for the tested angles of attack. For negative angles of attack, increased root-mean-square values indicate a highly unsteady flow environment at the uppermost pressure transducer. At positive angles of attack, the rotor wake impinges directly on the vertical tail, manifesting itself as significant pressure fluctuations PSD values at the first blade passing frequency. Furthermore, the maximum surface pressure fluctuation root-mean-square values, observed at various inflow angles exhibit distinct variations across the different rotor head configurations. The experiments are accompanied by numerical simulation and the rotor wake of the different rotor head variants are analyzed for selected angles of attack.

INTRODUCTION

Helicopter aerodynamics represents a highly complex discipline characterized by intricate flow phenomena such as dynamic stall, reverse flow regions, and compressibility effects. Furthermore, the rotor wake interacts with the fuselage, tail boom and horizontal and vertical stabilizers, consequently affecting the performance and stability of the helicopter.

Experimental and numerical simulations are essential tools to investigate and comprehend these unstable and complex effects, with the aim of enhancing helicopter performance, flight characteristics, and passenger comfort. Although the model size is not a limiting factor in numerical simulations, only a few test facilities such as the National Full-Scale Aerodynamics Complex (NFAC) 40- by 80-Foot Wind Tunnel, can accommodate full-size helicopters or rotors in experiments. Exemplary, Norman et al. (Ref. 1) performed full-scale investigations on a UH-60A rotor and the data were compared to flight tests in (Ref. 2).

Due to the helicopter size constraints, most experiments are performed on scaled and simplified helicopter models. When using scaled helicopter models, it is challenging to ensure the similarity of Reynolds number, Mach number, and advance ratio. Adjustments to the blade tip speed of the rotor and the wind tunnel's inflow velocity can achieve Mach number and advance ratio similarity. However, Reynolds number similarity on the rotor blades cannot be maintained. Therefore, helicopter investigations are mostly separated into two part problems: One investigation approach focuses on rotor blade aerodynamics according to similarity rules, while another examines helicopter performance utilizing truncated rotor blades or blade stubs. The latter approach models essential helicopter components, like fuselage, landing skids, tail boom, horizontal and vertical tail, in the wind tunnel to analyze the aerodynamic performance, including the interaction between rotor blade stubs and the fuselage and stabilizers.

Interactional aerodynamics between the main rotor and the tail rotor has been extensively studied. Sheridan (Ref. 3) monitored the flow field in front of the fin for various rotor configurations, investigating scenarios with the rotor head fully equipped with blades and hub, with only the hub and without the hub. Data collected from the flow field in front of the empennage exhibited a distinct four-per-revolution peak in the blade passage in the lateral flow angle time history. Additionally, a 1Ω frequency, associated with tail shake phenomena, was recorded. Sheridan's findings demonstrated that the rotor hub induces a notable increase in turbulence. However, the inclusion of rotating rotor blades resulted in a downward shift in the rotor wake and reduced turbulence levels within the measurement area.

Moedersheim (Ref. 4) conducted wind tunnel experiments on a 1:6 scaled helicopter with a generic fuselage shape and a T-tail empennage to explore rotor-tail interactions at various horizontal tail positions. The results indicated that for all advance ratios tested, the rotor wake passed below the high-tail configuration. In contrast, for the low tail arrangement, the rotor wake impinged directly on the T-tail at an advance ratio of $\mu = 0.25$. Investigations into the pressure distribution on the horizontal stabilizer, including both averaged and unsteady pressure fluctuations at various advance ratios, revealed maximum unsteady pressure fluctuations at the advance ratio of $\mu = 0.2$. However, further increase in the advance ratio diminished the amplitude strength and caused a phase shift in the pressure peaks.

Gorton et al. (Ref. 5) employed a 15 %-scaled helicopter model of the RAH-66 helicopter fuselage in a wind tunnel campaign to better understand rotor and fuselage interactions. Reich et al. (Ref. 6) provided a comprehensive summary of experimental and numerical investigations concerning rotor hubs. Shenoy et al. (Ref. 7) explored the scaling effects on a generic four-bladed hub through both experimental and numerical methods, performing simulations at different Reynolds numbers and comparing them with wind tunnel data. Further experimental studies by Reich et al. (Ref. 8) involved five distinct rotor hub geometries tested in a water tunnel, accounting for variations in Reynolds numbers and advance ratios. Moreover, in another study, Reich et al. (Ref. 9) conducted model-scale experiments to examine interactions between the rotor hub and engine pylon, utilizing stereo particle image velocimetry to capture the rotor hub wake. The investigation continued with a focus on the development of the hub wake until it reached the empennage (Ref. 10). De Gregorio et al. (Ref. 11) conducted an experimental study on a full helicopter model and analyzed the pitch-up and tail-shake phenomena. In addition, the study investigated the impact of the main rotor wake on the fuselage and tip vortices on the horizontal tail. Earlier investigations at the Technical University of Munich (Refs. 12,13) involves a five-bladed rotor head with blades truncated at the first aerodynamic section. Within these studies, the influence of the blade stubs on the overall drag was analyzed, as well as the hub cap vortex pairs and blade stub tip vortices were detected.

Previous research has investigated various rotor configurations, including full rotor blades, blade stubs, and hub-only configurations. These studies focused on the interaction between the rotor and the wake across different advance ratios and explored the flow field around the horizontal stabilizer. The current study aims to analyze the effects of high angles of attack on the flow field around the empennage. Further attention will be given to the development and interaction of the wake generated by different rotor heads, with varying blade lengths, and their impact on a T-tail empennage, utilizing transient pressure transducers mounted on the vertical tail.

Figure 1. Helicopter model with rotor head variant *R1* in the wind tunnel test section.

EXPERIMENTAL SETUP

This section introduces the experimental settings for the wind tunnel measurements, including the helicopter model and the pressure measurement technique. All measurements are performed with an advance ratio of $\mu = 0.35$ and a Reynolds number of about 0.5×10^6.

Wind Tunnel Facility and Wind Tunnel Helicopter Model

The experiments have been performed in the low-speed wind tunnel facility A of the Chair of Aerodynamics and Fluid Mechanics of the Technical University of Munich. The wind tunnel is constructed in a closed-return type. The test section has dimensions of $1.8\,\text{m} \times 2.4\,\text{m} \times 4.8\,\text{m}$ (height $\times$ width $\times$ length) and the experiments have been carried out in an open test section. The turbulence level of the wind tunnel facility is below 0.4 %, and the uncertainty in the spatial and temporal mean velocity distribution is less than 0.067 %.

The investigated helicopter wind tunnel model is a 1:7.33 scaled helicopter model of a characteristic twin-engine light (TEL) utility helicopter and is shown in Fig. 1. It consists of a fuselage, skid landing gear, mast fairing, rotor head, tail boom, and horizontal and vertical tail. The empennage is arranged in a T-tail configuration and no tail rotor is considered. This rotor model allows to investigate different blade shapes and blade lengths. The influence of different blade lengths on helicopter forces and moments was presented in previous studies by Hartmann (Ref. 14). In addition, the wake flow field was presented using Particle Image Velocimetry (PIV) measurements for an inflow angle of $\alpha = 0°$. The major focus in this study is on the occurring pressure distribution measuring on the vertical tail.
The three investigated rotor head variants are displayed in Fig. 2. On the left-hand side, the rotor head variant *R1* with the longest blade stubs is displayed and on the right-hand side, the shortest blades and the steering rods are detected. In the middle part of the figure, the medium blade stubs with the motor are shown. The size of blade stub *R1* is twice the diameter of the hubcap. The medium blade stubs (*R2*) reach a ratio of one in relation to the hubcap diameter. For the shortest rotor head variant, only the most-inner blade section with the pitch horn is modeled. This matches a blade length to hubcap ratio of 0.4.

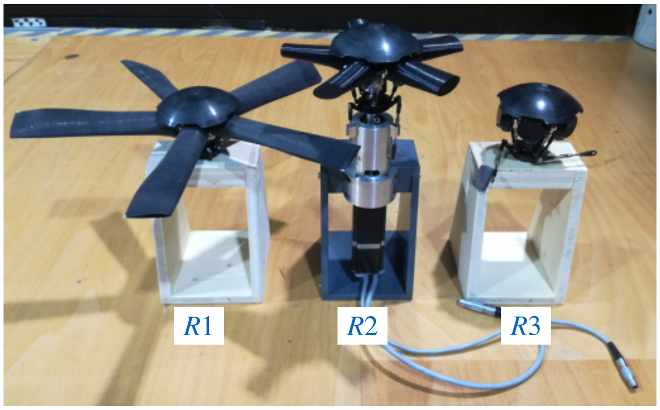

Figure 2. Rotor head variants *R1* (left), *R2* (middle) and *R3* (right).

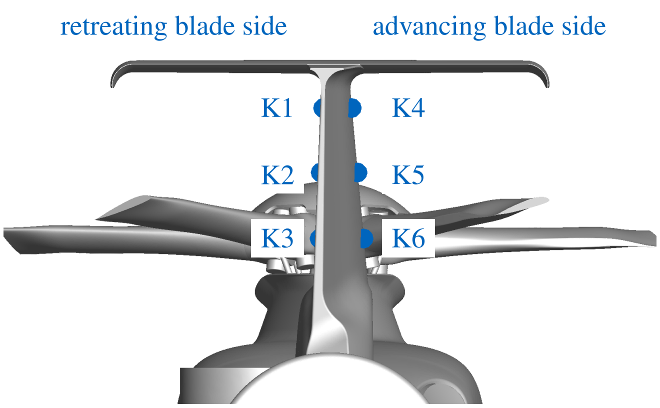

Figure 3. Position of the pressure transducer of rotor head variants *R1*.

Pressure Measurements

Transient pressure measurements have been performed to capture the pressure distribution on the empennage of the helicopter model. The pressure probes are located at the quarter-chord of the vertical tail. In total, six pressure transducers were installed, three on each side of the tail. The positions of the pressure transducers are shown in Fig. 3. The pressure probe located at the top of the vertical tail on the retreating blade side (pressure side) is labeled as *K1*, while the middle one as *K2* and the most bottom one *K3*. On the advancing side (suction side), the top located one is named *K4* and the other ones *K5* and *K6*, respectively. The top pressure probes are located just below the curvature of the horizontal tail mounting. The middle ones are as high as the hubcap while the lowest probes are at a level similar to the rotational center of the blades. The measurement matrix spreads from the angles of attack α of $-18°$ to $18°$ at an angle of sideslip $\beta = 0°$ with intermediate steps of $6°$. The measurement time is $t_t = 10\,\mathrm{s}$ and the sampling rate is $f_s = 5120\,\mathrm{Hz}$. A low-pass filter is applied at $0.45 \times f_s$ to avoid aliasing.

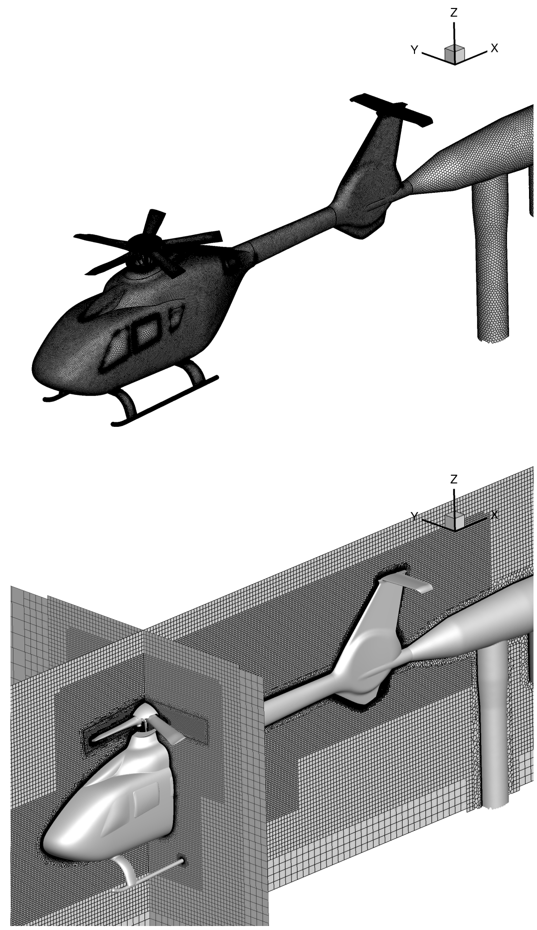

Figure 4. Surface mesh (top) and volume mesh (bottom) of the numerical helicopter model with rotor head $R1$.

NUMERICAL SETUP

The experimental investigations are complemented by numerical simulations. These simulations have been conducted on a scaled wind tunnel model of a helicopter using the commercial software ANSYS Fluent 2023R1. The analysis considers three different variants of the rotor head, each subjected to a range of inflow angles. The numerical grid was generated using ANSYS Fluent Meshing, producing an unstructured mesh composed of polyhedral and hexcore (poly-hexcore) elements. To accurately capture the rotor head's rotation, a sliding mesh interface was employed.

Figure 4 shows the resulting surface mesh of the helicopter with rotor head $R1$. In addition, two planes demonstrates the refinement boxes of the rotor wake. A y^+ value of approximately 1 was set at the walls in all domains to resolve the velocity gradient at the wall accurately.

The numerical setup employed in this study is analogous to the configuration presented in (Ref. 15). The computational mesh for the rotor head $R1$ simulations comprises approximately 40.6 million cells. Specifically, 27.4 million cells are allocated to represent the freestream domain and 13.2 million cells are utilized to model the flow field around the rotor head. Although the cell count for the freestream domain remains relatively constant, it varies for the different rotor head configurations. For the rotor head $R2$, the total numerical grid consists of 36.2 million cells, whereas the smallest rotor head, $R3$, has a grid comprising 34.6 million cells. A grid sensitivity study was performed for the helicopter with rotor head variant $R1$. The details of this study can be found in (Ref. 15).

The entire simulation is separated into two components. Initially, a steady-state simulation is executed to establish the flow field around the helicopter. In this phase, the turbulence is modeled using the k-omega SST model. Upon achieving a steady-state flow field, the solver was switched to the transient simulation mode, and the rotation of the rotor head is enabled. Consistent with the steady-state case, a pressure-based solver is utilized. In the transient simulation, the Scale-Adaptive Simulation (SAS) approach is employed to model the turbulence.

The rotor domain rotates at a rotational speed n employing the Mesh Motion approach in conjunction with the sliding mesh interface. A fixed time-step is calculated based on a one-degree azimuth resolution of the blade rotation.

NUMERICAL FLOW FIELD INVESTIGATION AT SELECTED ANGLES OF ATTACK

The interaction of the rotor wake with the vertical and horizontal tails is highly dependent on the inflow angle. Figure 5 illustrates the wake development of the numerical results from rotor head variant $R1$ for the angles of attack α of $-12°$, $0°$, $6°$ and $12°$.

The rotor wake is visualized by the turbulent kinetic energy (TKE) at a lateral axis slice through the rotor origin at an instantaneous time step for the rotor position, where one rotor blade is orientated towards the helicopter front. Additionally, the pressure coefficient c_p is depicted on the helicopter surface. For $\alpha = -12°$, no interaction between the rotor wake and the vertical tail is observed. The wake extends only to the end of the tail boom. However, the negative inflow angle at the horizontal tail results in high velocity and pressure fluctuations on the underside, which affects the uppermost pressure transducer. At $\alpha = 0°$, a rotor wake impinges on the empennage. However, the top located pressure transducer is not located in the direct wake of the rotor. With an increasing angle of attack, the rotor wake's influence on the fins becomes more pronounced. For $\alpha = 6°$, the wake departs from the rotor position almost horizontally and directly impinges on the vertical fin. At $\alpha = 12°$, the rotor wake is located further upstream and all pressure transducers are in the direct wake of the rotor.

For $\alpha = 0°$, the wake development of three rotor head configurations is analyzed along the tail boom. Figure 6 shows five cross-flow planes along the tail boom colored by the $c_{p,rms}$ values. In addition, the cross-flow plane is displayed at the downstream position of the top located pressure transducer. On the top, the flow field of the rotor head $R1$ is shown, in the middle $R2$ and in the bottom part $R3$.

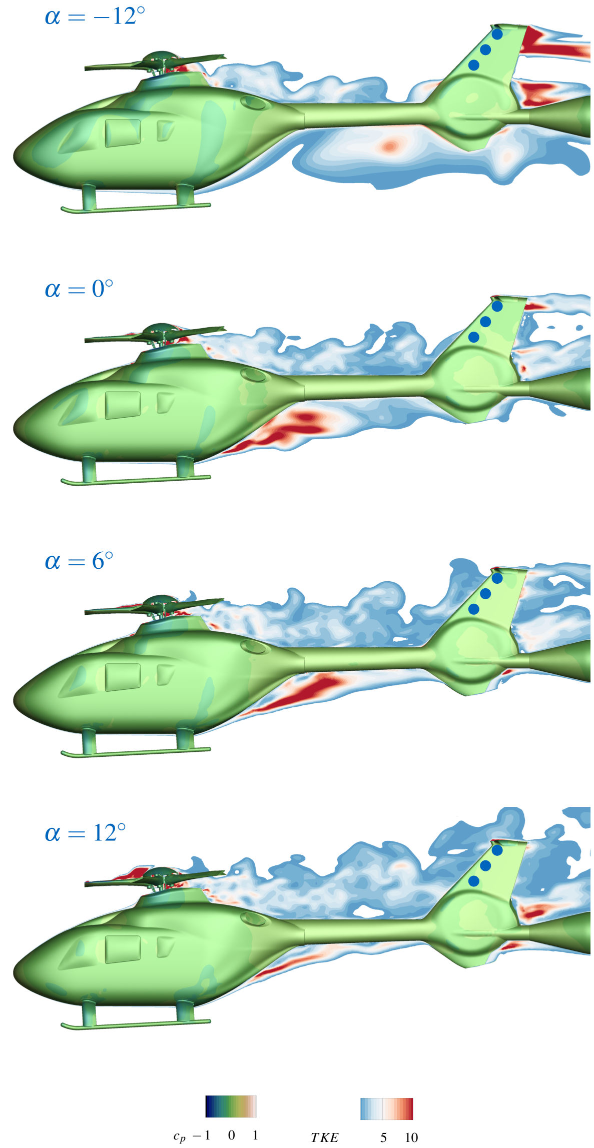

Figure 5. Rotor wake position for various inflow angles.

The first cross-flow plane behind the rotor exhibits a pressure field characterized by high $c_{p,rms}$ values centrally located above the tail boom. Specifically for rotor head $R1$, these high $c_{p,rms}$ values are predominantly found on the retreating blade side, whereas for $R2$ and $R3$, the high pressure fluctuations are more centrally localized. On the advancing blade side of $R1$, a distinct pressure peak is observed, directly attributed to the tip vortex. On the other side, a slight pressure peak is identified arising from the tip vortex of the retreating blade. These pressure peaks are absent for the smaller rotor heads, $R2$ and $R3$. Further downstream on the tail boom, the shape of the pressure field remains largely unchanged. Despite the high magnitudes of the pressure fluctuations across the entire plane for $R1$, the area characterized by high $c_{p,rms}$ diminished for $R2$ and $R3$. The pressure field through the vertical and horizontal tail indicates an increase in pressure at the lower fin section for all rotor heads. Comparing the cross-flow plane with the last plane on the tail boom reveals that the fin induces a slight reduction in $c_{p,rms}$ values on the retreating blade side. However, near the horizontal tail, the values of $c_{p,rms}$ increase again. These high $c_{p,rms}$ values significantly affect the pressure transducer located at the top. For rotor head $R1$, the $c_{p,rms}$ increase near the horizontal tail is more pronounced compared to rotor head $R2$ and $R3$, particularly just below the horizontal tail on the retreating blade side. On the advancing side of rotor head $R1$, the tip vortex remains distinctly identifiable and retains its strength. In contrast, no tip vortex traverses the empennage in the configuration that uses the rotor head $R2$ and $R3$.

Considering positive inflow angles, the high $c_{p,rms}$ fields behind the rotor are located further upwards and are interacting directly with the pressure transducers on the vertical tail. Furthermore, for positive angles of attack, the tip vortex on the advancing blade of $R1$ further influences the pressure transducers.

EXPERIMENTAL RESULTS

Pressure Coefficient $c_{p,rms}$ Values along Angles of Attack

The initial analysis focuses on the root-mean-square (rms) values of the surface pressure fluctuations given in nodimensional form by $c_{p,rms}$. Variations in these rms values with angle of attack are presented for different rotor head configurations.

Figure 7 illustrates the rms value of the pressure coefficient for the $R1$ rotor head at various angles of attack. The top figure displays the $c_{p,rms}$ values for the pressure probes located on the retreating blade side, while the bottom subplot shows the values for the advancing side. For large negative angles of attack, the pressure probes on the retreating blade side exhibit high $c_{p,rms}$ values. As the angle of attack increases towards $\alpha = 0°$, these rms values decrease. At this angle of attack, the pressure probe positioned at the bottom records the highest rms value. As the angle of attack continues to increase, the $c_{p,rms}$ value shows no significant change for the bottom pressure probes. However, the top pressure probe demonstrates a local maximum rms value at $\alpha = 6°$. On the advancing blade side, higher rms values are observed for positive angles of attack. However, at $\alpha = -12°$, a peak is detected for the pressure probe situated at the top. The maximum $c_{p,rms}$ value for the bottom pressure probe occurs at $\alpha = 6°$; for the top pressure probe, the maximum is reached at $\alpha = 12°$.

Flow separation at the leading edge of the vertical tail is responsible for high $c_{p,rms}$ values at negative angles of attack. The top pressure probe is additionally affected by the flow around the horizontal tail. Positive angles of attack result in increased $c_{p,rms}$ values due to fluctuating velocity and pressure components within the rotor wake. At $\alpha = 6°$ and $\alpha = 12°$, direct interactions occur between the rotor wake and the vertical tail.

Figure 8 displays the $c_{p,rms}$ values for rotor head $R2$ as determined from the pressure probes along the angle of attack. As observed with the rotor head $R1$, elevated $c_{p,rms}$ values are

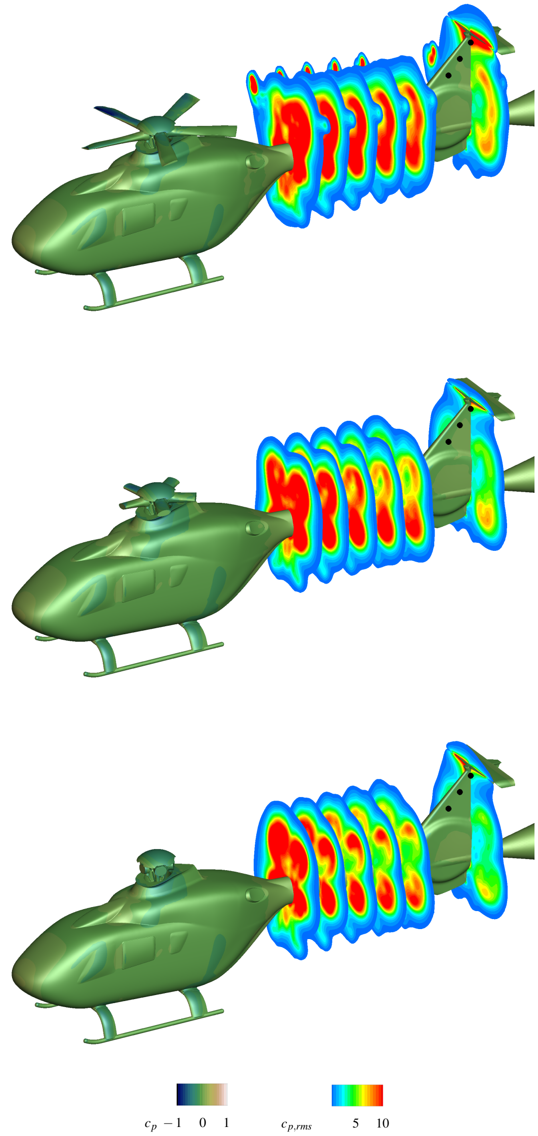

Figure 6. Cross-flow planes of $c_{p,rms}$ for rotor head $R1$ (top), $R2$ (middle) and $R3$ at $\alpha = 0°$

recorded for negative angles of attack on the side of the retreating blade, which are attenuated towards $\alpha = 0°$, reaching a minimum for the pressure probe located on the top. With increasing angles of attack, both bottom-located pressure probes remain relatively constant, while the top probe exhibits a local maximum at $\alpha = 12°$. The location of the maximum $c_{p,rms}$ value for rotor head $R2$ differs from that for $R1$, attributed to the shorter blade lengths impacting the site of peak pressure fluctuations. The shorter blades have an direct impact of the location of the maximum pressure fluctuations.

Moreover, the top pressure probe on the advancing blade side records a peak $c_{p,rms}$ at $\alpha = -12°$, consistent with the findings for $R1$. This consistency in location and magnitude indicates that the pressure fluctuations are principally influenced by the T-tail configuration, irrespective of the rotor head geometry. Low $c_{p,rms}$ values are observed at $\alpha = 0°$, while maximum values for the bottom pressure probes occur at $\alpha = 6°$. In

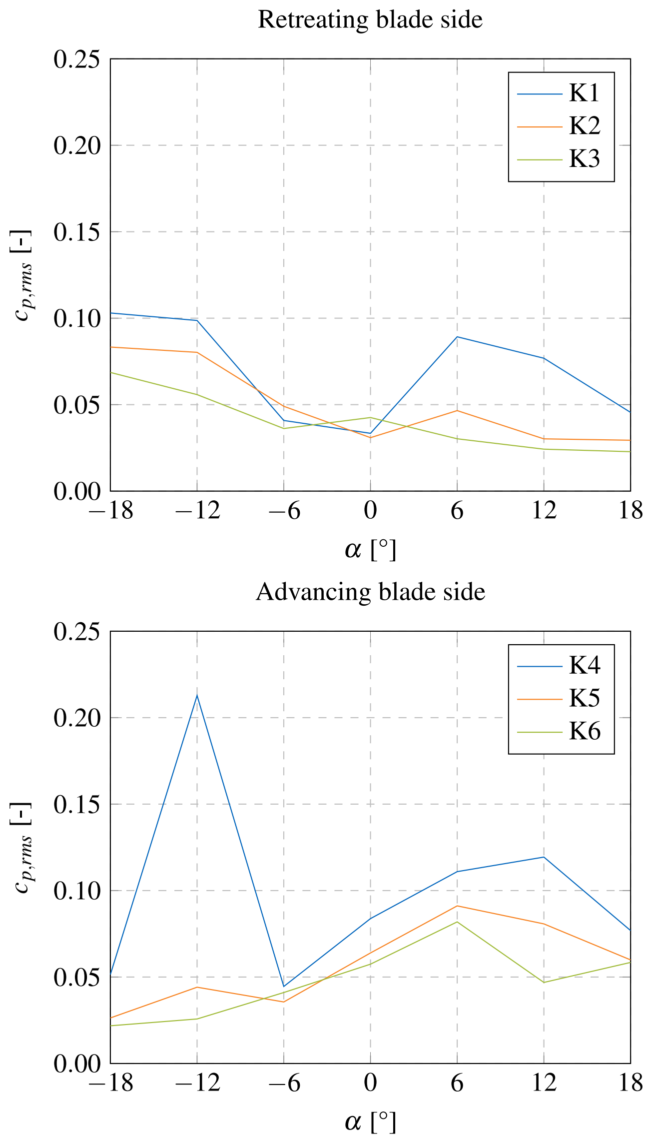

Figure 7. $c_{p,rms}$ **of rotor head** $R1$ **on retreating blade side (top) and advancing blade side (bottom).**

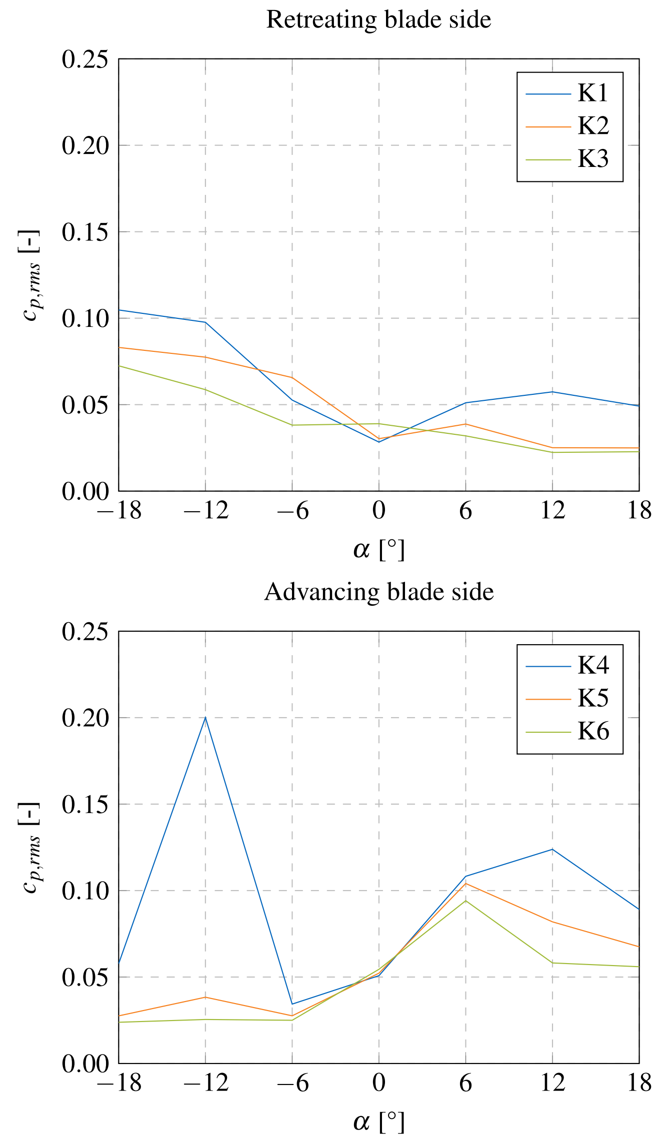

Figure 8. $c_{p,rms}$ **of rotor head** $R2$ **on retreating blade side (top) and advancing blade side (bottom).**

contrast, the top probe shows a local maximum at $\alpha = 12°$.

Figure 9 shows the $c_{p,rms}$ value obtained for rotor head $R3$. The retreating blade side pressure probes demonstrate raised $c_{p,rms}$ values at negative angles of attack. Specifically, the maximum rms value for the pressure probe located at the top is observed at an angle of attack, $\alpha = -12°$. At $\alpha = 0°$, all rms values match to a similar magnitude. As the angle of attack increases, the rms value for the bottom located pressure probes show minimal variations, whereas the rms value for the top located pressure probe peaks at $\alpha = 12°$.

The pressure probe on the advancing blade side exhibit behavior similar to that of $R1$ and $R2$ for negative angles of attack. Unlike $R1$, the maximum $c_{p,rms}$ value at $\alpha = 0°$ is detected by the bottom located pressure probe. The local maximum rms value for the top located pressure probe, in this case, occurs at $\alpha = 6°$, which deviates from the pattern observed in $R1$ and $R2$.

For negative angles of attack, the $c_{p,rms}$ values on the retreating blade side exhibit a similar behavior in all configurations. Specifically, at high negative angles of attack, the $c_{p,rms}$ value becomes increased due to flow separation on the horizontal and vertical tail. At $\alpha = 0°$, the magnitude of the $c_{p,rms}$ values remains within a comparable range for all rotor heads. When considering positive angles of attack, the peaks in the maximal $c_{p,rms}$ values demonstrate variability among rotor head variants $R1$, $R2$ and $R3$. Rotor head $R1$ achieves its peak $c_{p,rms}$ value at $\alpha = 6°$, whereas the smaller rotor heads, $R2$ and $R3$, reach their maximum values at $\alpha = 12°$. Additionally, rotor head $R1$ exhibits an approximately 35 % higher $c_{p,rms}$ value in comparison to both $R2$ and $R3$, while the difference between $R2$ and $R3$ is less than 1 %. Thus, the influence of the rotor head wake on the retreating side of the vertical tail is significantly noticeable for positive angles of attack.

On the advancing blade side, a global peak is evident across all rotor head configurations at an angle of attack, $\alpha = -12°$.

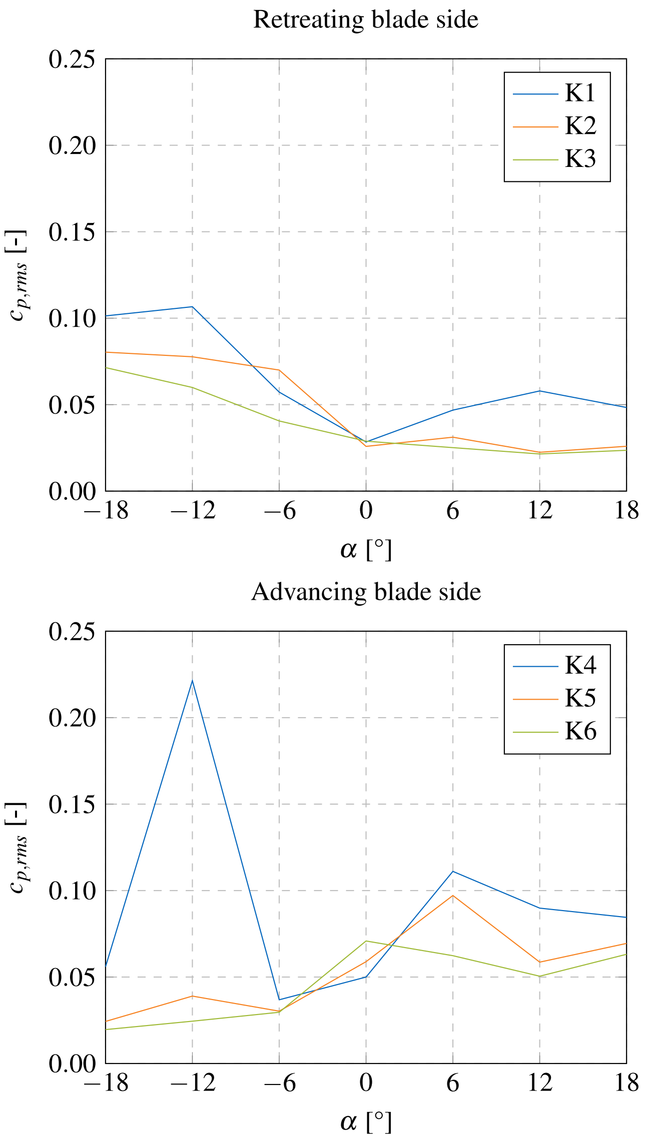

Figure 9. $c_{p,rms}$ **of rotor head** $R3$ **on retreating blade side (top) and advancing blade side (bottom).**

This peak is attributed to the flow separation on both the vertical and horizontal tail and is directly measured by the pressure probe located at the top. The maximum values fall within a range of $\pm 6\,\%$, indicating that the peak position is independent of the rotor head configuration. At $\alpha = 0°$, the top pressure probe recorded the highest value for rotor head $R1$, whereas for rotor head $R3$, the lowest pressure value was observed at the same probe location. For rotor head $R1$ and $R2$, the advancing side peak occurs at $\alpha = 12°$, while for rotor head $R3$, the peak is reached earlier at $\alpha = 6°$. Thus, the diverse geometries of the rotor heads significantly affect the positioning of the pressure peaks along the vertical tail, resulting in distinct impingement behaviors.

Pressure Power Spectral Density (PSD) at First Blade Passing Frequency

Gorton et al. (Ref. 5) characterized the positioning of the rotor wake by examining the vertical velocity component occurring at a frequency of four times per revolution, in front of the horizontal tail. Following a similar methodological framework, this study presents the power spectral density (PSD) of the pressure coefficient c_p' at the blade passing frequency f_{BPF}. This analysis enables the precise determination of the spatial position of the rotor wake and provides a quantitative measure of the pressure fluctuations generated by the rotor.

First, the pressure values of the rotor wake from rotor head $R1$ are investigated. Figure 10 shows the PSD values of the pressure probes located on the retreating blade side (top) and advancing blade side (bottom). At negative angles of attack, the PSD magnitude is generally low, indicating minimal interaction between the rotor wake and the T-tail. This is evident except for the minor peak observed in the power spectral density at $\alpha = -6°$ at the lowest pressure probe ($K6$) on the advancing blade side. For $\alpha = 0°$, the rotor wake impinges on the vertical tail, particularly affecting the top and middle pressure probes on the advancing blade side. Conserve, on the retreating blade side, the highest PSD value is measured at the lowest pressure probe. The PSD diagram reflects an asymmetry at $\alpha = 0°$ between the advancing and retreating blade sides, which is attributed to the difference in downwash angles generated by the rotor. The advancing blade side experiences a lower downwash, whereas the highest c_p' value in the PSD is recorded by the top pressure probe.
As the angle of attack increases, the rotor wake's interaction with the T-tail becomes more pronounced. The maximum PSD values on the retreating blade side occur at $\alpha = 6°$, while the peak PSD values on the advancing blade side are found at $\alpha = 12°$, both occurring at the top pressure probe. Beyond this, with higher inflow angles, the pressure component at the blade passing frequency decreases until it is minimized at 18°, where only a slight pressure PSD value at the rotor frequency is observed.

Figure 11 presents the pressure coefficient component at the blade passing frequency for the pressure probes, generated by rotor head $R2$. Across all inflow angles, the PSD values for $R2$ are generally lower than those generated by rotor head $R1$. At negative angles of attack, the pressure content is minimal, reaffirming the absence of interaction between the rotor wake and the T-tail. Specifically, at $\alpha = 0°$, an increase in BPF pressure is detected only on the advancing side, whereas the pressure magnitude on the retreating blade side remains constant. The highest PSD values occur at a 6° inflow angle on both sides, predominantly for the upper pressure probes. Notably, the advancing blade side exhibits higher PSD magnitudes than the retreating side, indicating wake influence across all pressure probes. At $\alpha = 12°$, the PSD values decreases again, showcasing a reduced wake effect on the T-tail. Further increases in inflow angle show no substantial interaction between the rotor wake and the T-tail.

Finally, the pressure coefficient component of the blade pass-

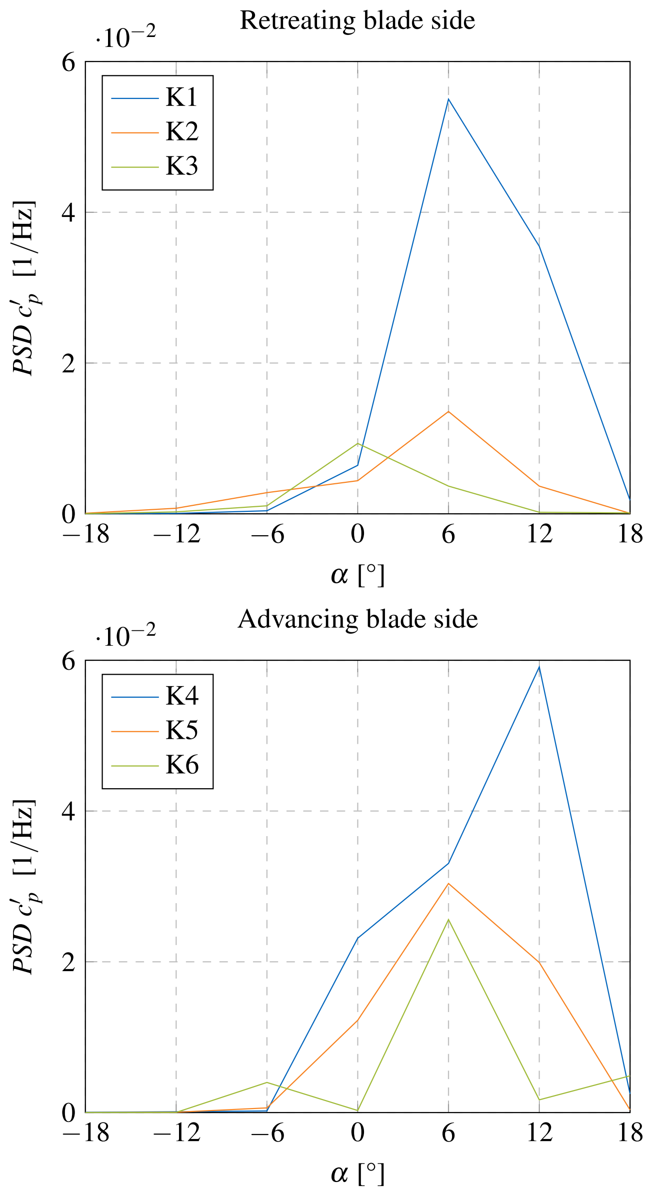

Figure 10. Power spectral density at first BPF for rotor head $R1$ on retreating blade side (top) and advancing blade side (bottom).

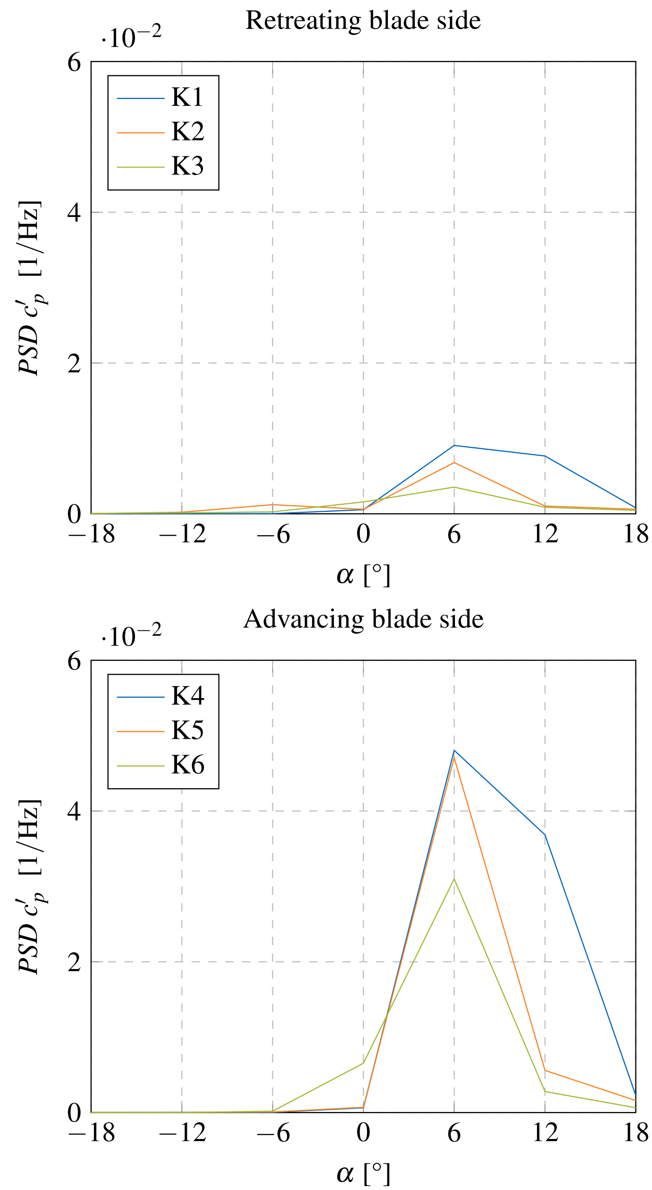

Figure 11. Power spectral density at first BPF for rotor head $R2$ on retreating blade side (top) and advancing blade side (bottom).

ing frequency for the smallest rotor head is depicted in Figure 12. For negative angles of attack, no pressure influence of the blade-passing frequency of the rotor wake is detected. For $\alpha = 0°$, there is no interaction on the retreating blade side, while on both bottom located pressure probes, an increase in the magnitude of the BPF component is observed. When $\alpha = 6°$, the uppermost pressure probe on the advancing side exhibits the highest PSD value. At 12°, the maximum pressure component occurs in the top probe on the retreating side. At 18°, the influence of the fifth-per-revolution content is reduced again.

For negative angles of attack, the rotor wake does not impact the T-tail, as the wake does not pass near the tail. Within the range of $\alpha = 0°$ to 12°, the rotor wake interacts with the empennage and a significant variation is observed between the rotor head variants. On the retreating blade side, rotor head $R1$ and $R2$ exhibits their maximum PSD values at an inflow angle of 6°, while $R3$ achieves its maximum at $\alpha = 12°$. Moreover, the pressure component magnitude of $R1$ is significantly higher compared to the smaller rotor head variants. Conversely, on the advancing blade side, the maximum PSD values for all rotor heads surpass those on the retreating blade side. Rotor head $R1$ reaches its peak at $\alpha = 12°$, while both smaller rotor heads attain their maxima at an inflow angle of 6°.

The peak pressure components of the blade passing frequency for rotor head $R1$ are similar between the advancing and retreating blade sides. However, for smaller rotor heads, a significant difference is detected between the advancing and retreating blade sides in terms of the top located pressure trans-

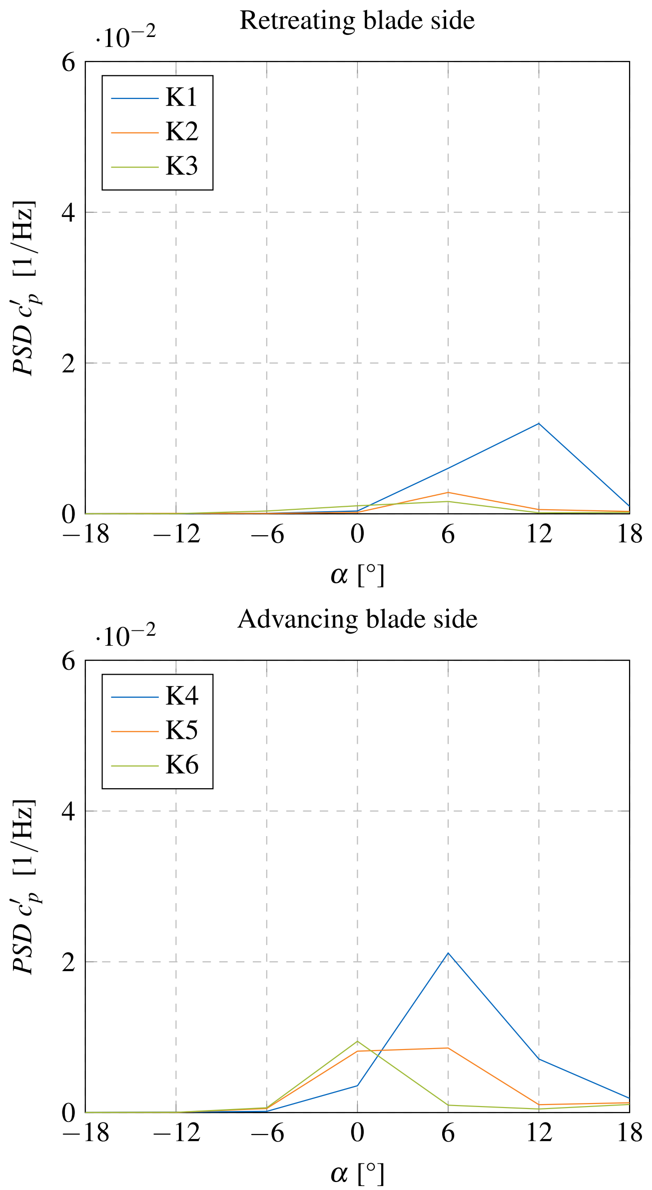

Figure 12. Power spectral density at first BPF for rotor head $R3$ on retreating blade side (top) and advancing blade side (bottom).

ducers.

Power Spectral Density of c_p' for Selected Angles of Attack

From the previous sections, it has been observed that the pressure transducer $K4$, located on the advancing side, exhibits the highest values of $c_{p,rms}$ and the most significant 5 per revolution pressure content. Consequently, the power spectral density (PSD) of c_p' is presented in this section for the frequency range of 10 Hz to 1000 Hz. The analyzes are performed for three different variants of the rotor head, assessed at angles of attack $\alpha = -12°$, $\alpha = 0°$, $\alpha = 6°$, and $\alpha = 12°$.

Figure 13 illustrates the PSD of c_p' at $K4$ for $\alpha = -12°$. At lower frequencies, the power spectral density across all rotor heads remains within a similar elevated range (approximately

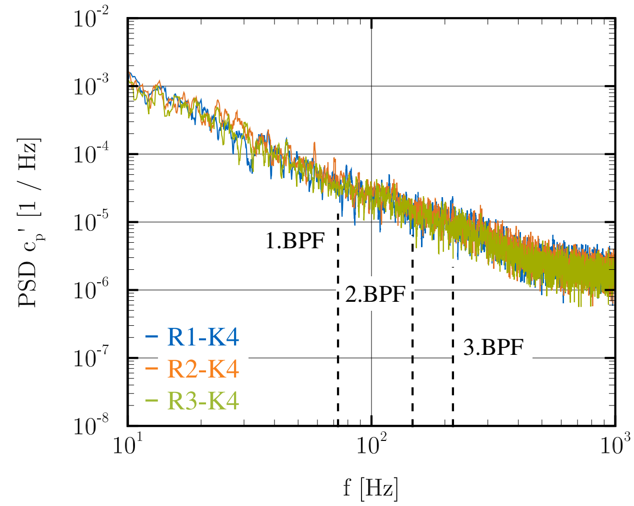

Figure 13. Power spectral density of c_p' for pressure transducer $K4$ at $\alpha = -12°$.

$\approx 1.0 \times 10^{-3}$). No distinct peaks are discernible at any frequency. For higher frequencies, the PSD exhibits a linear decrease. This decay follows the $-\frac{5}{3}$ decay for velocity turbulence spectra. This consistent behavior across the various variants of the rotor heads confirms the $c_{p,rms}$ values presented in the previous section (Figures 7, 8, 9), which demonstrate that the $c_{p,rms}$ values for different rotor heads are within the range of $\pm 6\,\%$.

Figure 14 presents the power spectral density of c_p' for the pressure transducer $K4$ at an angle of attack, $\alpha = 0°$. The PSD patterns of all three rotor heads demonstrate a similar trend. Starting at approximately 1.0×10^{-5} at low frequencies, PSD gradually decreases with increasing frequency. In general, the PSD level of rotor head $R1$ remains higher across the entire frequency spectrum compared to $R2$ and $R3$, which have comparable PSD levels. At the first blade passing frequency, all rotor head configurations exhibit a distinct peak. Although the PSD value for rotor head $R1$ is the highest, the smallest rotor head, $R3$, has a higher PSD value than $R2$. For the second BPF, the largest rotor head, $R1$, again shows the highest value, whereas the medium rotor head, $R2$, does not exhibit a discernible peak. Even at the third BPF, rotor head $R1$ induces a spectral peak.

The power spectral density of c_p' of $\alpha = 6°$ is illustrated in Fig. 15. At this inflow angle, the rotor head's influence is quite pronounced. The power spectral density values are comparatively lower at frequencies when juxtaposed with $\alpha = -12°$. However, numerous power peaks are discernible under these inflow conditions. The most prominent peaks occur at the first blade passing frequency f_{BPF} across all rotor heads. An additional peak is observed at the second BPF for all rotor heads. At the third BPF, a distinct peak is detected exclusively for the $R1$ and $R3$ rotor heads, whereas higher frequencies exhibit fewer PSD peaks. For rotor head $R1$, an additional peak in the power spectral density is identified at the fifth BPF. Additional PSD peaks are observed for all rotor head configu-

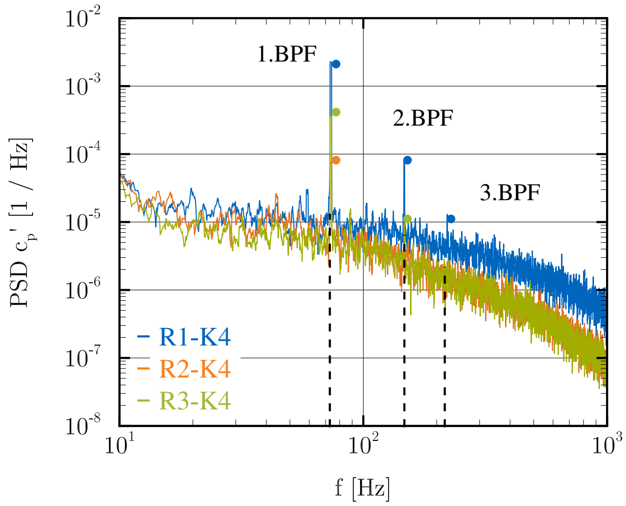

Figure 14. Power spectral density of c_p' for pressure transducer $K4$ at $\alpha = 0°$.

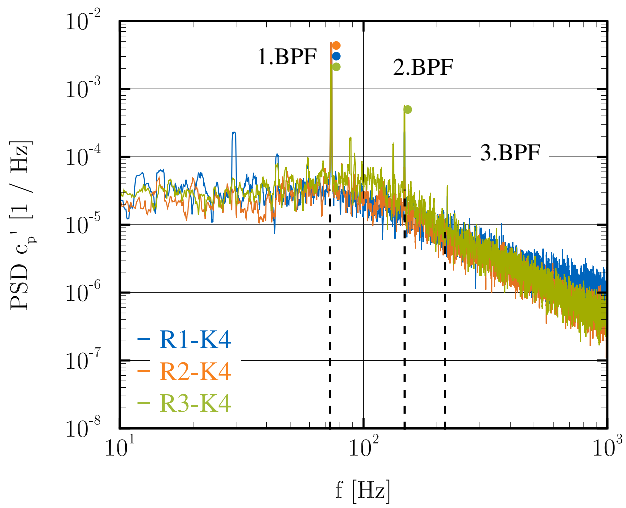

Figure 15. Power spectral density of c_p' for pressure transducer $K4$ at $\alpha = 6°$.

rations at frequencies lower than the BPF. These PSD peaks do not correlate with the blade passing frequency and may be caused by the wake of the fuselage and tail boom. Rotor head $R3$ has additional PSD values between the first and second blade passing frequencies that demonstrate greater fluctuations compared to other rotor heads.

Figure 16 shows the power spectral density for $\alpha = 12°$. For the rotor head variants $R1$ and $R2$, the values of $c_{p,rms}$ showed the highest levels at that angle of attack. The highest maxima are shown for all rotor head variants at the first, second, and third blade passing frequency by distinct peaks. At the harmonics of BPF, the magnitude of rotor head $R1$ is the highest, followed by $R2$ and $R3$. For higher frequencies, the PSD values are decreasing. At frequencies lower than f_{BPF}, few local maxima can be detected. Although there are no distinct maxima for the $R1$ rotor head, the medium and small rotor head variant shows some peaks.

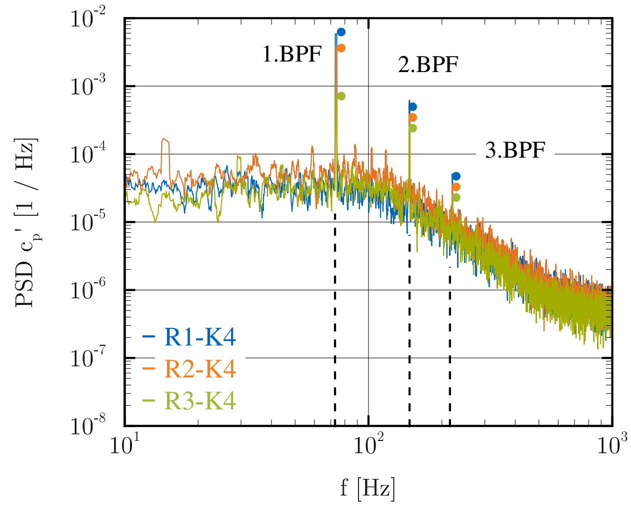

Figure 16. Power spectral density of c_p' for pressure transducer $K4$ at $\alpha = 12°$.

CONCLUSION

A detailed investigation of the impingement of the rotor wake on the empennage was performed for three different rotor head configurations, applying experimental and numerical results. For negative inflow angles, low power spectral density values indicates minimal interaction between rotor wake and T-tail. Conversely, increased positive $c_{p,rms}$ values reveal highly unsteady flow conditions around the pressure transducers ($c_{p,rms} = 0.21$ at $-12°$ for $K4$ and $R1$). At $\alpha = 0°$, the influence of the different rotor wake geometries begins to manifest in the pressure values. A distinct impact of rotor head geometry is observable at $\alpha = 6°$ and $\alpha = 12°$, where a clear interaction between the rotor wake and pressure transducers is evident. At 12°, the $c_{p,rms}$ fluctuations for rotor head $R1$ is 0.12, for $R2$ it is 0.12, and for $R3$ it is 0.09. Depending on the angle of attack, the rotor head exerts a significant influence on the flow around the horizontal and vertical tails. At moderate positive angles of attack, the maximum root-mean-square values, as well as the first harmonic of the blade passing frequency, exhibit distinct variations across different rotor head configurations. These diverse wake patterns affect the flow fields around the empennage, resulting in varied loading of the vertical and horizontal tail, ultimately impacting the overall performance of the helicopter.

ACKNOWLEDGMENTS

The funding of the presented investigation within the LuFo VI-2 project NANNY (iNNovative AN- uNd AuftriebssYsteme für die nächste Generation leichter bis mittelschwerer Hubschrauber, FKZ: 20Y2109) by the German Federal Ministry for Economic Affairs and Climate Action (BMWK) is gratefully acknowledged. Furthermore, the author deeply appreciate ANSYS for providing the flow simulation software. Moreover, the authors would like to thank the Gauss Centre for Supercomputing e.V. (www.gauss-centre.eu) for providing computing time on the GCS Supercomputer SuperMUC-NG at Leibniz Supercomputing Center (LRZ, www.lrz.de).

REFERENCES

1. Norman, T. R., Shinoda, P., Peterson, R. L., and Datta, A., "Full-Scale Wind Tunnel Test of the UH-60A Airloads Rotor," American Helicopter Society 67th Annual Forum, Virginia Beach, VA, May 2011.

2. Norman, T. R., Peterson, R. L., Maier, T. H., and Yeo, H., "Evaluation of Wind Tunnel and Scaling Effects With the UH-60A Airloads Rotor," American Helicopter Society 68th Annual Forum, Fort Worth, TX, May 2012.

3. Sheridan, P. F., and Smith, R. P., "Interactional Aerodynamics - A New Challenge to Helicopter Technology," *Journal of the American Helicopter Society*, Vol. 25, (1), January 1980, pp. 3–21. DOI: 10.4050/JAHS.25.1.3.

4. Moedersheim, E., and Leishman, J. G., "Investigation of Aerodynamic Interactions Between a Rotor and a T-Tail Empennage," *Journal of the American Helicopter Society*, Vol. 43, (1), 1998, pp. 37–46. DOI: doi:10.4050/JAHS.43.37.

5. Gorton, S. A., Berry, J. D., Hodges, W. T., and Reis, D. G., "Rotor wake study near the horizontal tail of a T-tail configuration," *Journal of Aircraft*, Vol. 39, (4), 2002, pp. 645–653.

6. Reich, D., Shenoy, R., Smith, M., and Schmitz, S., "A review of 60 years of rotor hub drag and wake physics: 1954–2014," *Journal of the American Helicopter Society*, Vol. 61, (2), 2016, pp. 1–17. DOI: 10.4050/JAHS.61.022007.

7. Shenoy, R., Holmes, M., Smith, M. J., and Komerath, N. M., "Scaling Evaluations on the Drag of a Hub System," *Journal of the American Helicopter Society*, Vol. 58, (3), 2013, pp. 1–13. DOI: 10.4050/JAHS.58.032002.

8. Reich, D., Willits, S., and Schmitz, S., "Scaling and Configuration Effects on Helicopter Rotor Hub Interactional Aerodynamics," *Journal of Aircraft*, Vol. 54, (5), 2017, pp. 1692–1704. DOI: 10.2514/1.C034250.

9. Reich, D., Sinding, K., and Schmitz, S., "Visualization of a helicopter rotor hub wake," *Experiments in Fluids*, Vol. 59, 2018, pp. 1–12. DOI: 10.1007/s00348-018-2571-7.

10. Reich, D. B., Elbing, B. R., Berezin, C. R., and Schmitz, S., "Water Tunnel Flow Diagnostics of Wake Structures Downstream of a Model Helicopter Rotor Hub," *Journal of the American Helicopter Society*, Vol. 59, (3), 2014, pp. 1–12. DOI: 10.4050/JAHS.59.032001.

11. De Gregorio, F., Pengel, K., and Kindler, K., "A comprehensive PIV measurement campaign on a fully equipped helicopter model," *Experiments in fluids*, Vol. 53, 2012, pp. 37–49.

12. Grawunder, M., Reß, R., Stein, V., Breitsamter, C., and Adams, N. A., "Validation of a Flow Simulation for a Helicopter Fuselage Including a Rotating Rotor Head," New Results in Numerical and Experimental Fluid Mechanics X: Contributions to the 19th STAB/DGLR Symposium Munich, Germany, 2014, 2016.

13. Stuhlpfarrer, M., Kümmel, A., and Breitsamter, C., "Investigations of Helicopter Wake Flow Including Rotor-Head Motion," *Journal of Aircraft*, Vol. 55, (5), 2018, pp. 2114–2126. DOI: 10.2514/1.C034689.

14. Hartmann, U., Ruhland, J., and Breitsamter, C., "Wind Tunnel Analysis of Helicopter Aerodynamics with Varying Rotor Head Blade Stub Lengths," New Results in Numerical and Experimental Fluid Mechanics XIV, edited by A. Dillmann, G. Heller, E. Krämer, C. Wagner, and J. Weiss, 2024. DOI: doi:10.1007/978-3-031-40482-5_58.

15. Hartmann, U., and Breitsamter, C., "Helicopter Rotor Wake Investigations on a Wind Tunnel Model with Varying Blade Stub Lengths," FORUM 2023-Vertical Flight Society 79th Annual Forum and Technology Display, 2023.